Hindawi
Mathematical Problems in Engineering
Volume 2017, Article ID 5279790, 14 pages
https://doi.org/10.1155/2017/5279790

Research Article

A Comparison of Classical and Pulsating Jets in Crossflow at Various Strouhal Numbers

Jianlong Chang,[1,2] Xudong Shao,[3] Jiangman Li,[4] and Xiao Hu[2]

[1]*College of Mechatronic Engineering, North University of China, Taiyuan, China*
[2]*School of Aerospace Engineering, Beijing Institute of Technology, Beijing, China*
[3]*Beijing Institute of Space Systems Engineering, Beijing, China*
[4]*State Power Investment Corporation Shanxi New Energy Co., Ltd., Taiyuan, China*

Correspondence should be addressed to Jianlong Chang; changjianlong1989@126.com

Received 25 December 2016; Accepted 30 January 2017; Published 23 February 2017

Academic Editor: Yannis Dimakopoulos

Investigation of the classical and pulsating jet in crossflow (JICF) at a low Reynolds number (Re = 100) has been performed by the LES method based on varied velocity ratios (r = 1~4). Time-averaged particle trajectories are compared in the classical and pulsating JICF. The formation mechanism and the corresponding flow characteristics for the counter-rotating vortex pair (CRVP) have been analyzed. An unexpected "vortex tail" has been found in the JICF at higher velocity ratio due to the enhanced interactions indicated by the increased jet momentum among the CRVP, upright vortices, and shear layers. The analysis of time-averaged longitudinal vorticity including a coupling mechanism between vortices has been performed. The returning streamlines appear in the pulsating JICF, and two extra converging points emerge near the nozzle of the jet at different Strouhal numbers. The temperature profiles based on the iso-surface for the classical and pulsating JICF have been obtained computationally and analyzed in detail.

1. Introduction

The jet in crossflow (JICF) is an essential flow phenomenon which is used in many aerospace engineering and environmental applications for efficient dispersion of the species [1, 2]. The flow dynamics of a JICF is a typical flow problem which always involves many basic turbulent mixing issues [3]. The impact of geometry and flow configuration (velocity ratio, turbulence, inclination angle, temperature, etc.) on jet trajectory, scalar mixing, the morphology of structures, and other flow phenomena on the JICF have been investigated in previous research [4–28].

Hsu and Huang [4] had conducted experiments to study the effects of acoustic excitation on the flow behavior, penetration, and the spread of stack-issued, wall-issued transverse jets. The corresponding results had shown that the excited transverse jets with the swinging motion and traveling puffs could create larger penetration height and spreading width compared with the nonexcited jet. The formation of vortex rings in negatively buoyant starting jets had been studied numerically by Marugán-Cruz et al. [5] based on different Richardson numbers. The vorticity distribution in the vortex rings had shown different behaviors in the two regimes after pinching off from the trailing stem. Serials of the flow behaviors and velocity field of an oscillating jet in a crossflow had been also investigated by Hsu et al. [6]. The results had shown that the wavy flow structure in the phase-averaged vorticity contour was characterized by two adjacent vorticity-concentrated areas of opposite signs. The positive vortices could be generated on the leeward side of the wavy flow structure due to the counterclockwise-rotating vortices formed on the leeward side shear layer. However, the negative vortices would be formed on the leeward side of the wavy flow structure (positive vorticity denotes a counterclockwise rotation and negative vorticity, a clockwise rotation).

Camussi et al. [7] had proved that the establishment of different behaviors at various velocity ratios can be interpreted physically due to the effect of the Reynolds number and velocity ratios for the jet. This signified that Reynolds number and velocity ratios had an essential effect on the destabilization mechanisms for the mixed vortices formation.

Cadirci et al. [8] had demonstrated the performance of a zero-net-mass-flux Jet and Vortex Actuator (JVA) in the 2D-crossflow flat-plate laminar boundary layer. It was clear that the boundary layer velocity profiles were significantly affected by the JVA-induced flow regimes at different operating frequencies. The JVA was proved to be an effective way to delay or prevent the possible laminar boundary layer separation which might further occur downstream in an area of adverse pressure gradient. Bagheri et al. [9] had performed the linear stability analysis for the jet in crossflow at a jet-to-crossflow velocity ratio of 3 by self-sustained global oscillations. The most unstable global modes with high frequencies were compact, and the corresponding modes represented localized wave packets on the CRVP, which were associated with the loop-shaped vortical structures near the jet shear layer. Lim et al. [10] had drawn the conclusion that the trajectories of circular jets in crossflow can be scaled with rd (d is the nozzle diameter and r is the jet-to-crossflow velocity ratio), whereas the flow dynamics for elliptic ring-like vortices demonstrated that it may not collapse the elliptic jet trajectories in the same way as a circular jet. New [11] had carried out the experiment for elliptic jets in crossflow with the aspect ratio (AR) of the nozzle from 0.3 to 3. The corresponding results had shown a stronger flow reversals for the higher aspect ratio, where the formation of more intense counter-rotating vortex pair over the low-aspect-ratio elliptic jets will not appear. Yuan et al. [12] had reported on a series of large eddy simulations for a round jet in crossflow. Simulations were performed at two Reynolds numbers (1050 and 2100, resp.). The results had shown that the adopted LES method was accurate.

One of the primary effects on the flow field of a JICF is the velocity ratio r [22]; if the densities in the jet and the crossflow are the same, r can be defined as

$$r = \frac{V_{\text{jet}}}{V_{\text{crossflow}}}. \tag{1}$$

Here, V_{jet} is the jet velocity; $V_{\text{crossflow}}$ is the velocity of the crossflow. If the densities in the jet and the crossflow are different, the effective velocity ratio r can be obtained by the square root of the momentum flux ratio as

$$r = \sqrt{\frac{(\rho V^2)_{\text{jet}}}{(\rho V^2)_{\text{crossflow}}}}, \tag{2}$$

where ρ_{jet} is the density of the jet fluid and $\rho_{\text{crossflow}}$ is the crossflow fluid density.

It is well known that a pulsating or synthetic jet can be passively affected by Strouhal number (St), which can be defined as

$$\text{St} = \frac{f \cdot L}{V}, \tag{3}$$

where f is the frequency, L is the characteristic length, and V is the fluid velocity. Turbulence and penetration data had shown that the responses of spread and penetration seemed to be optimal at St = 0.22 [4].

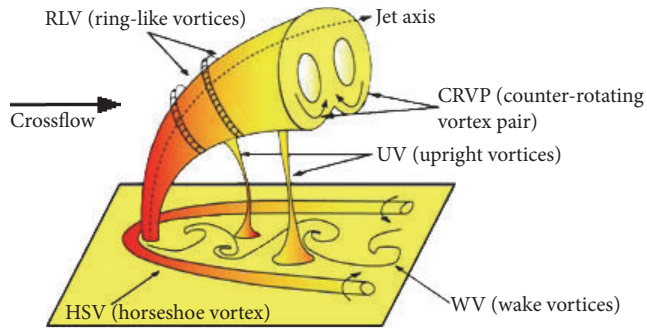

Figure 1: Vortex structures of JICF [13].

As shown in Figure 1 [13], five types of large vortex structures are detected in the JICF: the counter-rotating vortex pair (CRVP), the horseshoe vortex (HSV), the wake vortices (WV), the upright vortices (UV), and the ring-like vortices (RLV), which have a great influence on ejected jet control. It is greatly important to clarify the mechanism for the generation of large-scale coherent structures in the proposed development.

From an overall viewpoint, the experiments conducted by Camussi et al. [7] had shown that the principal vortical systems in JICF were the same as those obtained at larger Reynolds numbers. Vortex rings at low Reynolds number are clearer and more stable, which contributes to the investigation and analysis of JICF. And large eddy simulation at low Reynolds number had been performed [12], the corresponding results computed from the simulations had been proved to match experimental measurements reasonably well. It signifies that large eddy simulation also has an excellent performance at low Reynolds number.

Therefore, large eddy simulation and analysis for a jet in crossflow at low Reynolds number (Re = 100) with various Strouhal numbers ranging within 0.11~0.33 will be performed in this paper. The jet-to-crossflow velocity ratios (r) vary from 1 to 4.

2. Flow Configuration and Numerical Methods

2.1. Flow Configuration and Grid Distribution. The domain in the jet in crossflow is shown in Figure 2. The centerline of the round jet is located 6.5D away from the crossflow boundary, where D is the diameter of the round jet. The spatial scope of the vertical direction is sixteen times the jet dimension; then the length is sixty-five times the diameter of the jet in the streamwise direction. And the width is twenty times the jet dimension in the spanwise direction. All the simulations conducted by Fluent are performed at r = 1~4. For the Reynolds number, the diameter of the round jet is defined as the characteristic length, the characteristic velocity is the velocity of the crossflow, and the fluid medium is water.

The whole flow domain will be divided into several cells. The mesh is structured along x-, y-, and z-axis directions and will be refined near the entrance of jet. The grid distribution in the computational domain by the front view has been shown in Figure 3. The impacts of various velocity profiles

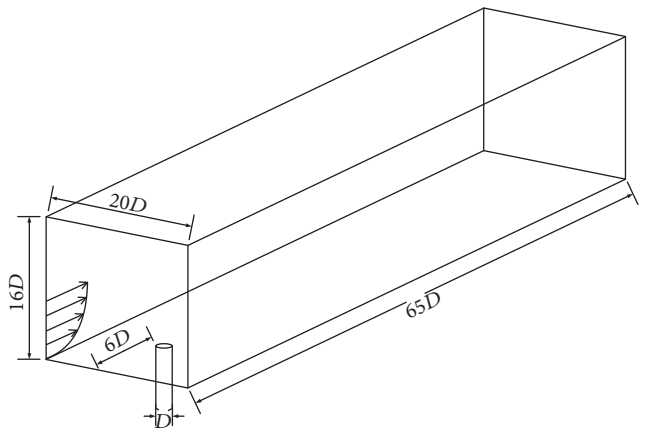

Figure 2: Domain in the jet in crossflow.

Table 1: Different cases list.

Case	Velocity ratio	Strouhal number
C1	1	—
C2	2	—
C3	3	—
C4	4	—
C5	1	0.11
C6	2	0.11
C7	3	0.11
C8	4	0.11
C9	1	0.22
C10	2	0.22
C11	3	0.22
C12	4	0.22
C13	1	0.33
C14	2	0.33
C15	3	0.33
C16	4	0.33

and Strouhal numbers on the flow field are investigated at Re = 100. C1~C4 are classical JICF cases; the others are for pulsating JICF. The studied cases have been listed in Table 1.

It is necessary to explain the velocity profile for the pulsating JICF in this paper. As an example, the profile of the jet velocity at the jet nozzle for C12 is shown in Figure 4, in which the ordinate is the value of $V_{\text{jet}}/V_{\text{crossflow}}$. The profiles of the jet velocity generate a periodic oscillation at the jet entrance. Different from the conventional pulsating jet, the velocity magnitude of pulsating jet conducted in the simulation is always no less than zero. The velocity at the jet nozzle is oscillating with the dimensionless time $t_{\text{flow}} = t/T$, where t is the flow time starting from the pulsating jet and T is the oscillating period. The time-averaged velocity for the pulsating jet is defined as the effective velocity. Hence, the corresponding velocity ratio for C12 is $r = 4$.

2.2. Numerical Method. Large eddy simulation (LES) has been adopted in this paper, which is different from Reynolds Averaged Navier-Stokes Equation (RANS) and Direct Numerical Simulation (DNS). The aim of the LES is to resolve the larger scale of turbulence, and the smaller ones are modeling based on the universality. The key idea of LES is to limit the computational cost by only solving the larger scales of the flow while modeling the smaller ones. By filtering process in LES, the vortices less than a certain scale will be filtered from the flow field, and large eddy will be calculated firstly. Then the solution of small eddy will be captured by solving additional equation. Consequently, LES is more suitable for industrial applications. In the case of JICF, the unsteady behavior of the various flow structures is expected to be important, and the unsteady LES approach which provides spatiotemporal resolution can be used [23].

For LES, the flow will be divided into the large-scale eddy and small-scale eddy. The basic equations of LES can be obtained after filtering Navier-Stokes equation and the continuity equation [24, 25]:

$$\begin{aligned} \frac{\partial\left(\rho\overline{u_i}\right)}{\partial t} + \frac{\partial\left(\rho\overline{u_i u_j}\right)}{\partial x_j} &= -\frac{\partial\overline{p}}{\partial x_i} + \frac{\partial}{\partial x_j}\left(\mu\frac{\partial\overline{u_i}}{\partial x_j}\right) - \frac{\partial\tau_{ij}}{\partial x_j}, \\ \frac{\partial\rho}{\partial t} + \frac{\partial\left(\rho\overline{u_i}\right)}{\partial x_i} &= 0, \end{aligned} \tag{4}$$

where ρ is the density of fluid, u_i and u_j are the velocity components, p is the pressure, μ is the kinematic viscosity coefficient, and the variables of formula with an overline are the field variables filtered. Component of subgrid stress tensor is $\overline{\tau_{ij}} = -\rho(\overline{u_i u_j} - \overline{u_i}\,\overline{u_j})$, showing the motion effect of small eddy to large eddy. And u_i is defined as $u_i = \overline{u}_i + u_i'$; therefore, the subgrid stress can be decomposed into three parts as

$$\begin{aligned} \tau_{ij} &= \overline{u_i u_j} - \overline{u}_i\overline{u}_j = \overline{\left(\overline{u}_i + u_i'\right)\left(\overline{u}_j + u_j'\right)} - \overline{u}_i\overline{u}_j \\ &= \overline{\overline{u_i}\,\overline{u_j}} - \overline{u}_i\overline{u}_j + \overline{\overline{u}_i u_j'} + \overline{u_i'\overline{u}_j} + \overline{u_i' u_j'} \\ &= L_{ij} + C_{ij} + R_{ij}, \end{aligned} \tag{5}$$

where L_{ij} is Leonard stress of the subgrid stress and stands for the motion effect among the solvable large eddy, which can be obtained by $L_{ij} = \overline{\overline{u_i}\,\overline{u_j}} - \overline{u_i}\,\overline{u_j}$. The cross stress of the subgrid stress stands for the motion effect between the solvable large eddy and the unsolvable small eddy, which can be computed as $C_{ij} = \overline{\overline{u}_i u_j'} + \overline{u_i'\overline{u}_j}$. R_{ij} is the interaction among the unsolvable small eddy captured by $R_{ij} = \overline{u_i' u_j'}$.

The relationship between $\overline{\tau_{ij}}$ and $\overline{S_{ij}}$ which is on behalf of the components of the strain rate tensor can be expressed as $\overline{\tau_{ij}} - (1/3)\delta_{ij}\overline{\tau_{kk}} = -2\nu_T\overline{S_{ij}}$. ν_T is turbulent viscosity, δ_{ij} is Kronecker symbol, and $\overline{S_{ij}}$ is strain rate tensor after filtering,

$$\overline{S_{ij}} = \frac{1}{2}\left(\frac{\partial\overline{u_i}}{\partial\overline{x_j}} + \frac{\partial\overline{u_j}}{\partial\overline{x_i}}\right). \tag{6}$$

Turbulent viscosity μ_T can be configured as product between length scale l and velocity scale q. Assuming that the

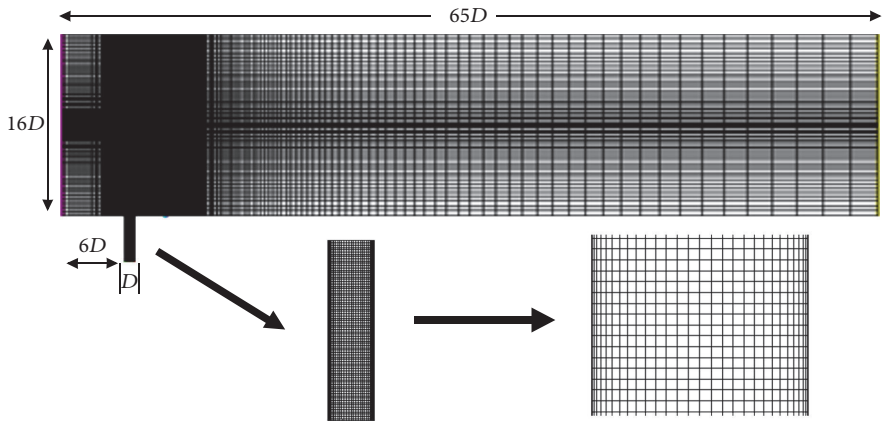

Figure 3: Grid distribution in the computational domain by the side view.

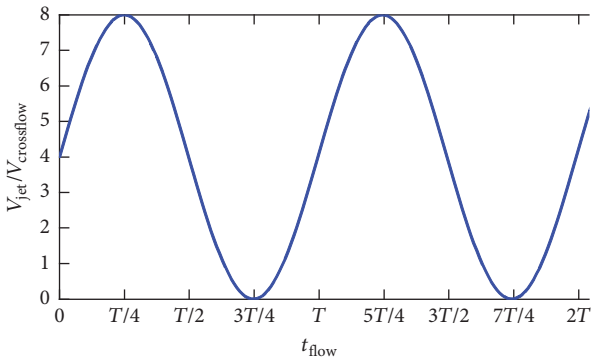

Figure 4: Velocity profile for C12.

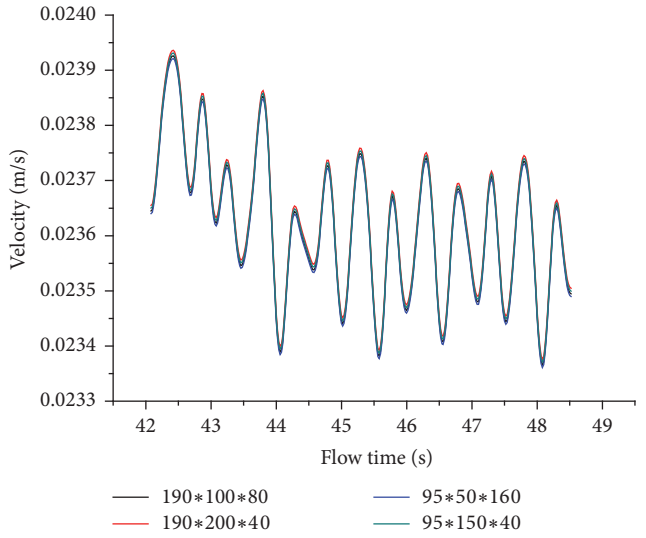

Figure 5: Grid sensitivity test.

magnitude of small-scale is in equilibrium, length scale and velocity scale can be defined as $l = C_s\overline{\Delta}$, $q = \overline{\Delta}|\overline{\mathbf{S}}|$; then the turbulent viscosity μ_T can be expressed as

$$\mu_t = l^2 \left|\overline{\mathbf{S}}\right|, \tag{7}$$

where C_s is constant of Smagorinsky, and the approximation of the constant can be obtained by $C_s \approx (1/\pi)(3C_k/2)^{-3/4}$.

The value measured in the atmosphere for Kolmogorov constant is 1.4; thereby $C_s \approx 0.18$. However, the value of C_s is usually taken as 0.1 in practical application. $\overline{\Delta}$ is the scale of grid filter, and it is obtained by $\overline{\Delta} = (\Delta x \Delta y \Delta z)^{1/3}$. For unstructured grids, $\overline{\Delta}$ could be acquired by extracting a cube root for the unit volume. $\overline{\mathbf{S}}$ can be captured by $|\overline{\mathbf{S}}| = \sqrt{2\overline{\mathbf{S}}_{ij}\overline{\mathbf{S}}_{ij}}$.

3. Results and Discussion

3.1. Test of the Grid Sensitivity and Time Step. The grid sensitivity is tested and the corresponding results are displayed in Figure 5. We have chosen four different grid types ($A * B * C$) for the numerical simulation. A, B, and C are the nodes in the streamwise, spanwise, and vertical direction, respectively. As shown in Figure 5, it is found that the deviation of the studied grid types is within 1%. Subsequently, 190 * 100 * 80 type is adopted in the following simulations.

In the numerical simulations, time steps have great effect on the accuracy. Longer time steps can result in lower accuracy, while the shorter ones will cause unnecessary waste of computing resources. Hence, the sectional vorticity in the JICF is tested for the verification of time step. The instantaneous vorticity at the same moment, with the same Reynolds number and velocity ratio but different time steps at $x = 3D$, is shown in Figure 6. The results presented in Figures 6(a) and 6(b) indicate that the vorticity is almost the same for the various time steps of 0.005 s and 0.0025 s, and the corresponding results of the two time steps have high consistency. After comprehensive consideration, time step in the paper will be fixed at 0.005 s.

3.2. Time-Averaged Particle Trajectory. Figure 7 shows different time-averaged particle trajectories of the classical and pulsating JICF obtained from the LES data. The trajectories show that the jet is deflected downstream by the action of the crossflow. In the proximity of the nozzle for the jet, it is found that the time-averaged particle trajectories are

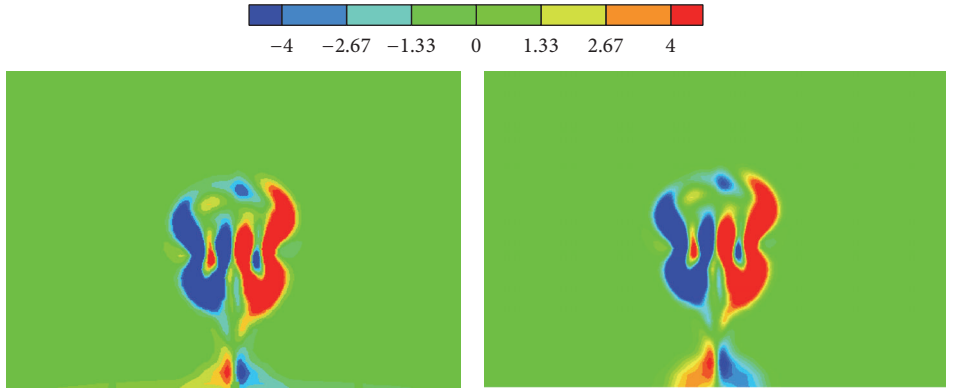

Figure 6: The instantaneous vorticity at $x = 3D$ ((a) time step = 0.005 s; (b) time step = 0.0025 s).

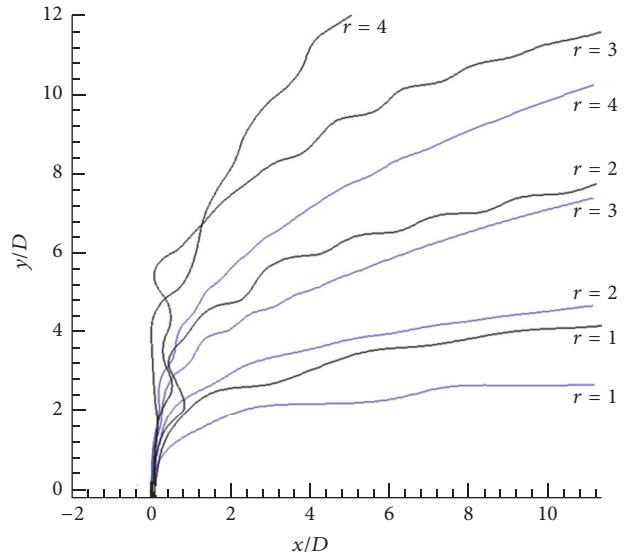

Figure 7: The time-averaged particle trajectories for the classical and pulsating JICF (blue line for C1~C4, black line for C9~C12).

almost vertical up to the crossflow. The trajectories show that the fluids in the nozzle exit of the jet interact with the crossflow fluid, as it deviates away and begins to curve in the direction of the crossflow [26]. The complex vortices will begin to be generated, such as the counter-rotating vortex pair, upright vortices, ring-like vortices, horseshoe vortex, and wake vortices.

Figure 7 compares the time-averaged particle trajectories extracted from the simulation. It reveals that the corresponding jet penetrates higher for the higher velocity ratio, and the penetration is almost followed by r. The time-averaged particle trajectories of jets at different velocity ratios will differ significantly, which is because of variable coactions between the jet and the crossflow boundary layer thickness. It is clear that the penetration and unsteady time-averaged particle trajectories of the pulsating JICF can be generated actually higher than the classical JICF. The reason is the effect of the velocity profiles in the pulsating JICF. Comparing the velocity profiles of the classical and pulsating JICF, it is obvious that the effects of velocity profile for the pulsating JICF will generate enhanced velocity magnitudes in the lower positions of the JICF. And the magnitude of the velocity profile in the upper position of the JICF will experience minor changes. Therefore, the magnitude of the velocity for the pulsating cases will become larger and more stable in the near field. The deflection of the pulsating JICF can demonstrate a higher penetration. Another significant phenomenon is that the trajectories of the pulsating JICF have shown constantly curved performance in the near field; the higher the velocity ratio, the more the curves the trajectory generate. The velocity profile of the pulsating will always change with the periodic performance, which generates relatively unstable curves in the near field.

The numerical results in the paper will be validated with the experimental results as follows. A dimensional analysis neglecting the effect of Reynolds was performed in the research [27], and the conclusions were summarized as the following trajectory form:

$$\frac{y/D}{r} = A\left(\frac{x/D}{r}\right)^{b}, \tag{8}$$

where y/D is the height of the penetration, x/D presents the corresponding streamwise location, and r is the velocity ratio. Pratte and Baines [27] successfully resolved b near 0.28, and the value of the coefficient A showed a variation ranging from 1.35 to 2.63. The time-averaged particle trajectories of the C1~C4 are shown in Figure 7 (blue lines), and the corresponding coefficient A is 1.54, 1.49, 1.58, and 1.79, respectively, which are in good agreement with the results [27]. The coefficient b is obtained from the simulation data; the values of b are 0.25, 0.26, 0.28, and 0.30, respectively, which are in agreement with the experimental results [27]. Overall, the agreement between numerical and experimental results [27] is excellent, which shows that LES is also of higher accuracy at low Reynolds numbers.

Figure 8 shows the time-averaged particle trajectories for the pulsating JICF at various Strouhal numbers. The velocity profiles yield obvious results for the pulsating cases

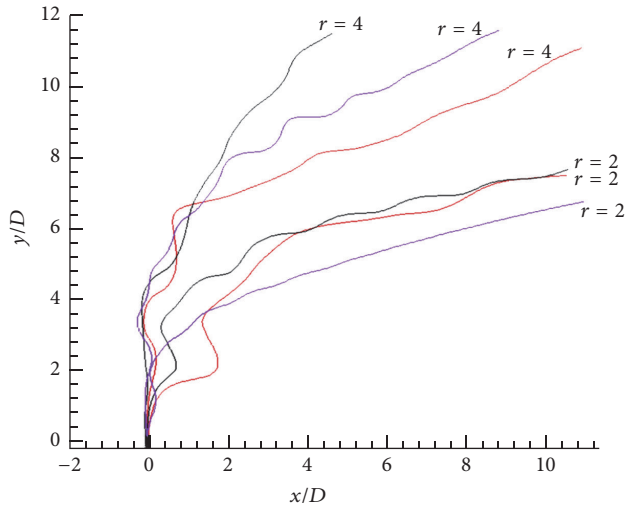

Figure 8: The time-averaged particle trajectories for the pulsating JICF at various St (purple: St = 0.33, black: St = 0.22, and red: St = 0.11).

Table 2: Coefficients A and b for various cases.

Case	A	b
C6	1.96	0.25
C8	2.01	0.23
C10	2.47	0.24
C12	2.62	0.31
C14	1.99	0.28
C16	2.30	0.25

with different Strouhal numbers; the results clearly reveal that the performance of higher velocity ratios shows the deeper penetration than the lower ones. Without considering curving in the near field, the trajectories listed in Figure 8 can be fitted by (8). The coefficients A and b in the (8) are displayed in Table 2. The coefficient A ranges from 1.96 to 2.62, and the coefficient b ranges from 0.22 to 0.31, which can show good agreement with the experiment results [27]. It demonstrates that the time-averaged particle trajectories of the pulsating JICF are also consistent with (8).

3.3. Flow Pattern. Figure 9 shows the typical instantaneous flow patterns in the side view for the classical and pulsating JICF under different velocity ratios (C1~C4 and C9~C12) after full development, so that readers can obtain better understanding of the vortex rings for JICF. The most significant large-scale vortex structures observed in JICF are CRVP and RLV. Figure 9(a) shows the side view of CRVP and RLV along with the component of spanwise vorticity contours; a leading vortex ring as indicated in Figures 9(a) and 9(e) begins to arise near the round jet entrance in the transverse jet. As shown in Figure 9(a), the leading vortex ring deforms, enlarges, becomes less coherent, and travels downstream with a vortex chain trailing behind [4]. On the one hand, the leading vortex ring can generate the evolution subsequently to the downstream region. On the other hand, the leading vortex ring will be followed by a series of upstream vortices which are created during the jet evolution process under the interaction in the shear layer between the jet and crossflow. As shown in Figure 10, the mechanism for the formation of CRVP is that the eddy flows are decomposed due to the impact of pressure gradient near the entrance of the jet. Under the pressure gradient, the vortex diameter will be expanded rapidly, and a pair of counter-rotating vortex appears along the JICF direction. After a long evolution, it is obvious that the large-scale vortex structures of CRVP and RLV in Figure 9 manifest weaker along with the wake region. At low velocity ratios ($r = 1$ and 2) as shown in Figures 9(a), 9(b), 9(e), and 9(f), the wake vortices in horizontal surface are more apparently associated with the upright vortical structures in both classical and pulsating JICF.

At the higher velocity ratios, the generation, evolution of vortex structures, and the interactions are significantly affected by the varied velocity ratios. The flow characteristics of the vortices strongly depend on the velocity ratio (r). While the velocity ratio becomes larger ($r \geq 3$) as shown in Figures 9(c), 9(d), 9(g), and 9(h), RLV will only last a shorter distance due to the coactions between CRVP, UV, and shear layer. The frequency of RLV will increase with the increasing of velocity ratio. With the augment of velocity ratio, the jet kinetic energy increases. The gap of RLV near the nozzle will be generated closer, and the diameter for RLV will become smaller. However, due to the strong interaction of WV, HSV, UV, RLV, and shear layer with high kinetic energy, RLV will be destroyed in a very short time. The horseshoe vortex appears ahead of the jet nozzle, which seems to be identical for all the four cases with a stable performance.

By comparing the vorticity contours for the same velocity ratio, the vorticity of the pulsating JICF is more complicated in Figure 9. More RLV will appear in the pulsating JICF, and the gap of the corresponding RLV will become closer than for classical ones. This phenomenon is caused by the velocity profiles of the pulsating jet. The velocity of the pulsating JICF is under cyclical fluctuation, which would be more conducive to the generation of flow characteristics. And an unexpected generated vortex "vortex tail" appears at the higher velocity ratio in Figures 9(c), 9(d), 9(g), and 9(h), which are clearer in the pulsating JICF. The most important reason for the emergence of the vortex tail in the process of JICF is due to the enhanced coactions among the CRVP, upright vortices, and shear layer. On the leeward side of JICF, a turbulence wake similar to Karman vortex street will shake off along the trail. The interaction between the turbulence wake and CRVP not only can increase the height of CRVP but also can generate the wake of the CRVP. The vortex tail is slender in the classical JICF displayed in Figures 9(c) and 9(d), and it is connected closer to the CRVP. For the pulsating JICF at $r = 3$ shown in Figure 9(g), the vortex tail has been mixed in the CRVP and RLV. And in another pulsating JICF (Figure 9(h)) at the velocity ratio $r = 4$, there is a clear separation between CRVP and vortex tail. This is because the velocity of the pulsating JICF is always changing with an unsteady characteristic, which results in the separation.

In the paper by Haven and Kurosaka [28], the noncircular holes had made it possible to reveal the unexpected

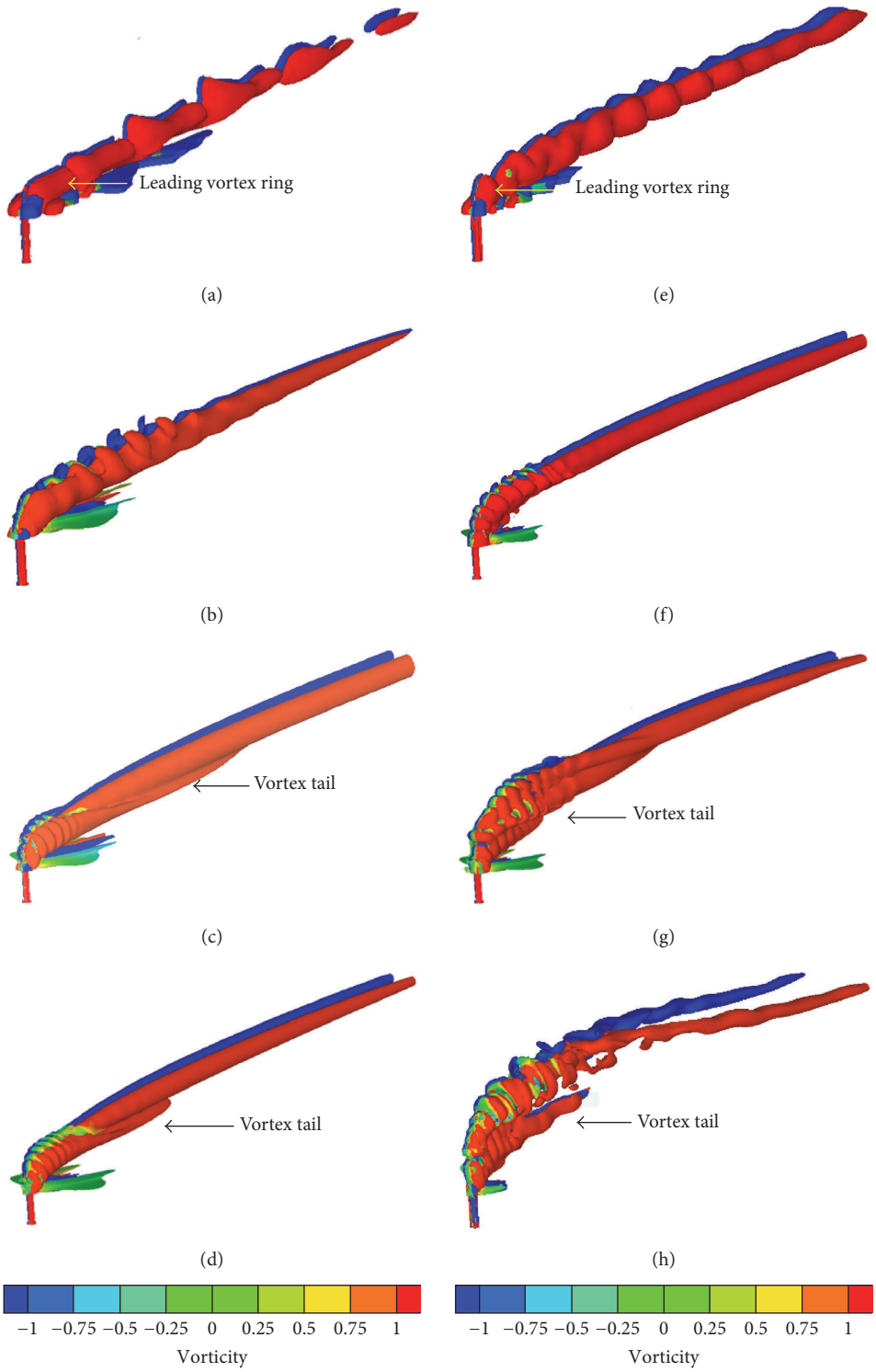

Figure 9: Instantaneous 3D contours of vorticity magnitude for eight cases ((a) C1, (b) C2, (c) C3, (d) C4, (e) C9, (f) C10, (g) C11, and (h) C12).

double-decked structures of streamwise vortices and link them to the vorticity generated along the wall of the hole. The double-decked structures of streamwise vortices were shown in Figure 11.

The lower-deck vortices are termed "steady," although they are perturbed by the unsteadiness of the upper deck. The sense of rotation of the "steady" lower deck is the same as the kidney vortices. With the increase of the aspect ratio, the distance between the left and right borders of the steady kidney vortices will increase. The upper-deck vortices (unsteady vortices) ride intermittently over the top of the steady ones. The rotation direction of the upper-deck vortices

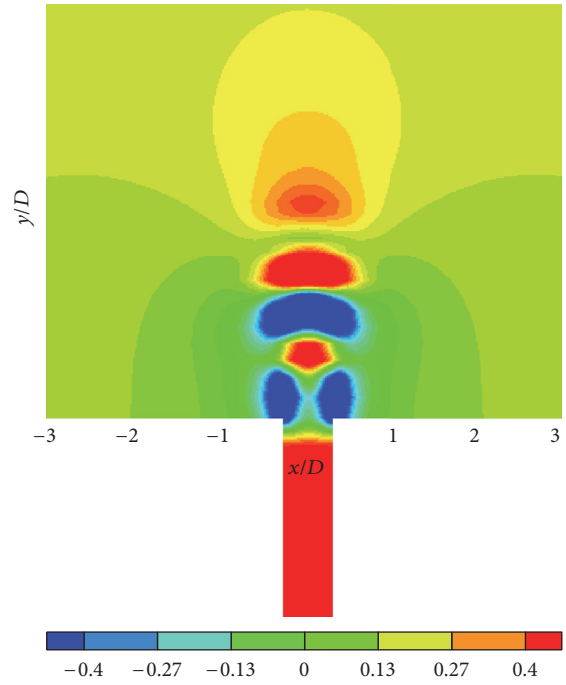

FIGURE 10: Pressure gradient at $x = 0.02D$.

varies with the aspect ratio. The rotation direction of unsteady kidney vortices in Figure 11(a) is opposite to the one in Figure 11(b). The unsteady kidney vortices for low-aspect-ratio rectangular, elliptical, square, and round holes are shown schematically in Figure 11(a). The unsteady antikidney vortices for high-aspect ratio elliptical and rectangular holes are shown in Figure 11(b). Different from the results of Haven and Kurosaka [28], the steady kidney pairs in this paper are all located in the upper-deck position. The magnitude of the unsteady vortices is far less than the vortices by Haven and Kurosaka [28]. Most importantly, vortex tail is not rotating. This characteristic is completely different from the double-decked structures in the research of Haven and Kurosaka [28]. What is more, as discussed above, there is a clear separation between CRVP and vortex tail at $r = 4$ in the pulsating JICF.

Figure 12 is an overall view of vortex structure in the pulsating JICF at Re = 100 with $r = 4$ and St = 0.22. In this discussion, the evolution of the vortex tail will be expounded. Near the nozzle, the vortex tail has appeared due to the action between pulsating jet and crossflow. While once produced in the beginning, vortex tail will not immediately fall off but stretch under CRVP and RLV. Vortex tail can generate a gradual rising in the interaction among the small-scale vortices (HSV, UV, and WV) and boundary layer. As shown in Figure 12(a), vortex tail is generated near the nozzle. With the increasing distance from the nozzle, the scale and magnitude of vortex tail are enhancing (Figures 12(a)–12(e)). During the development, vortex tail is discontinuous along the jet axis. With the further development of the pulsating JICF, the intensity of vortex tail will be evolved stronger, and vortex tail will start to fall at a certain time after deformation and distortion as shown in Figure 12(f). After full evolution, vortex tail will be generated more stable, and the corresponding length is shorter.

3.4. Analysis of Time-Averaged Longitudinal Vorticity. Comparison of the time-averaged longitudinal vorticity at $x = 6D$ for the four cases ((a) C4, (b) C8, (c) C12, and (d) C16) is shown in Figure 13, where early evolution of the JICF appears. In the initial stages of the development for JICF, the large-scale vortex structures still contain CRVP and RLV, UV, and WV near the vicinity of the jet field exit. Other small-scale structures can also be observed in Figure 13, and evolution of all the vortices remains essentially symmetrical.

For case C4 as shown in Figure 13(a), the penetration is lowest in the studied four cases, which is corresponding to the results (Section 3.2). For the cases of jet with pulsating velocity profile (Figures 13(b), 13(c), and 13(d)), the vertical rise of the CRVP is observed to be higher. The kidney-shaped vorticity in Figure 13(a) is the smallest due to the uniform velocity profile reducing the coactions between vortices. The vortex tail is not apparent in the C4, while the vortex tail appears under different Strouhal numbers in C8, C12, and C16. For the pulsating cases, both CRVP and RLV have undergone significant separation. The vortices are more complicated, and the magnitude of the corresponding vorticity has also been enhanced. In the vorticity contours of JICF, there will be some coupling between the positive and negative vortex structures. And with the increase of velocity ratio, the coupling between positive and negative vortex structures will be reinforced. In C4 and C12, the gap between positive and negative vortex structures is very small, and there is almost no positive vorticity generated in the left half of Figure 13(c), while in C8 and C16, the positive and negative vortex structures are mixed. The C12 at the Strouhal number 0.22 has performed well in the coupling effect of positive and negative vortex structures among all the pulsating JICF at $r = 4$.

The CRVP of a round JICF can generate a stable performance for C4, C12, and C16, while the CRVP for C8 has shown the difference. The reason is that the cycle for the velocity profile of the C8 is longer than the others, and the relatively larger interval of the velocity profiles can result in unstable CRVP. In Figure 13, RLV for the pulsating JICF is thicker than the classical JICF. RLV for the pulsating JICF in C8 and C16 demonstrates significant unstable interaction; more positive vortices appear in the left half of Figures 13(b) and 13(d). A comparison of vortex tail for different cases has shown that the vortex tail can be generated from the initial stage of the JICF in the pulsating cases. For lower Strouhal number (St = 0.11), there is a latent interaction among the CRVP, RLV, and vortex tail. At the greater Strouhal number (St = 0.33), the shape of vortex tail will become slender compared with Figure 13(c). The magnitude of the vortex tail at $r = 4$ seems to be optimized at St = 0.22.

3.5. Phase-Averaged Velocity Fields Near the Nozzle. The formation of near-field large-scale vortices not only has an effect on the crossflow entrainment and jet trajectories but also can affect the evolution of CRVP [29]. The research

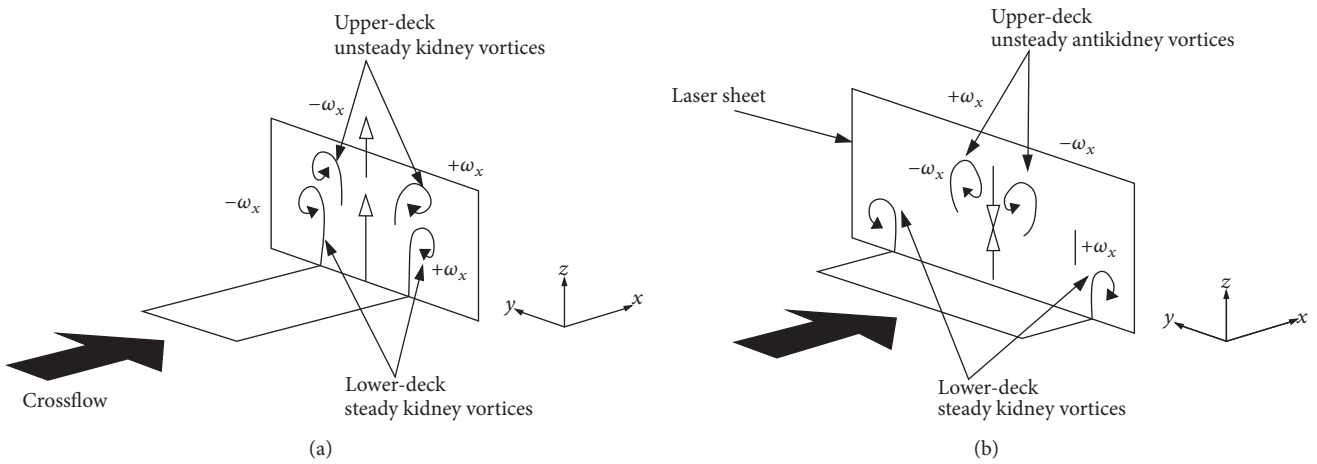

FIGURE 11: Double-decked structure showing (a) unsteady kidney pair in the upper deck for low-aspect-ratio rectangle and (b) unsteady "antikidney" pair for high-aspect ratio rectangle [28].

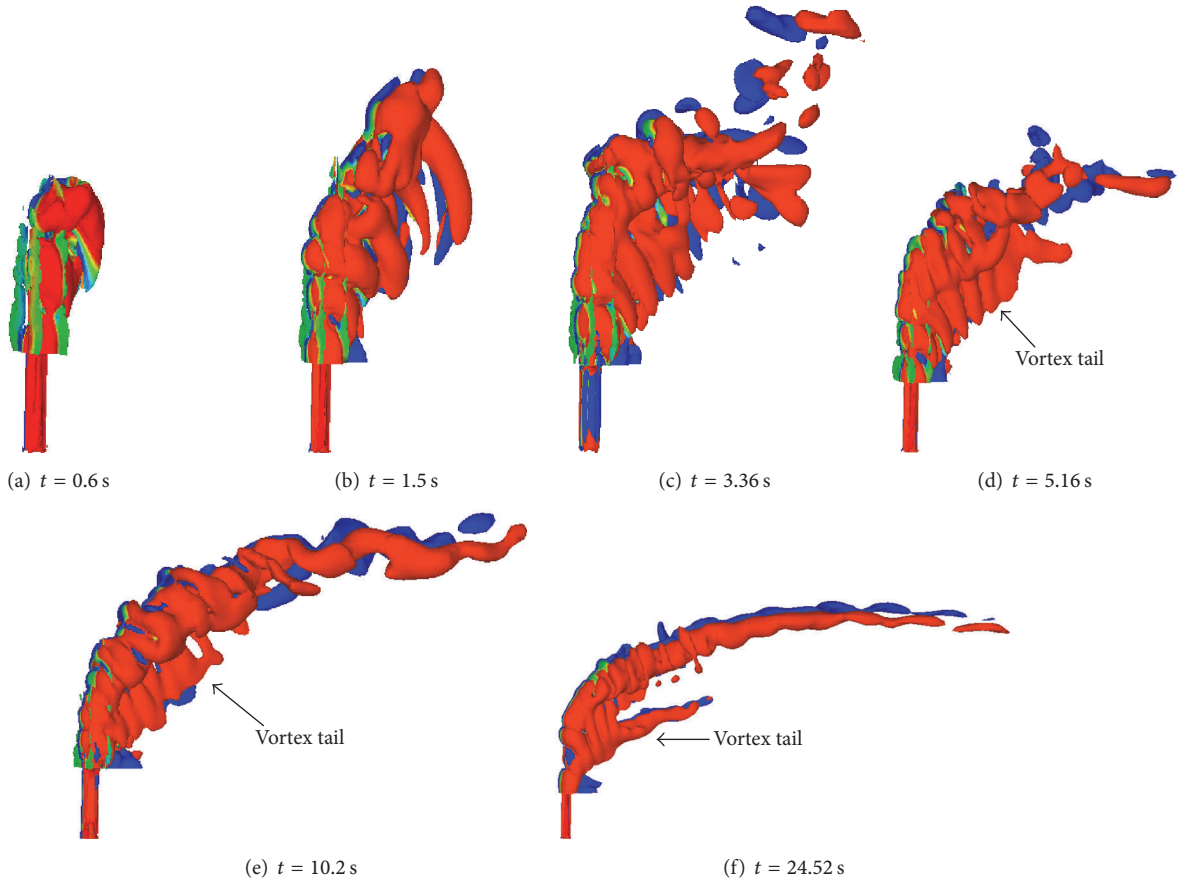

FIGURE 12: Evolution of vortex tail for pulsating JICF.

on the start and development of CRVP at present can be attributed to the coefficient results of coactions between the velocity profile for initial jet and the successive action of the crossflow. The phase-averaged velocity fields near the nozzle at $r = 4$ for four cases are presented in Figure 14. The section of streamlines is plotted at $y = 0$.

At the start of JICF as shown in Figure 14, the streamlines evolved from the nozzle in the near field are curved by the crossflow. The streamlines near the nozzle move up vertically and flow directly into the downstream zone. With the increasing distance along the x-axis direction (x/D), the jet-exit streamlines will get closer at $x/D \approx 1.5$, and the

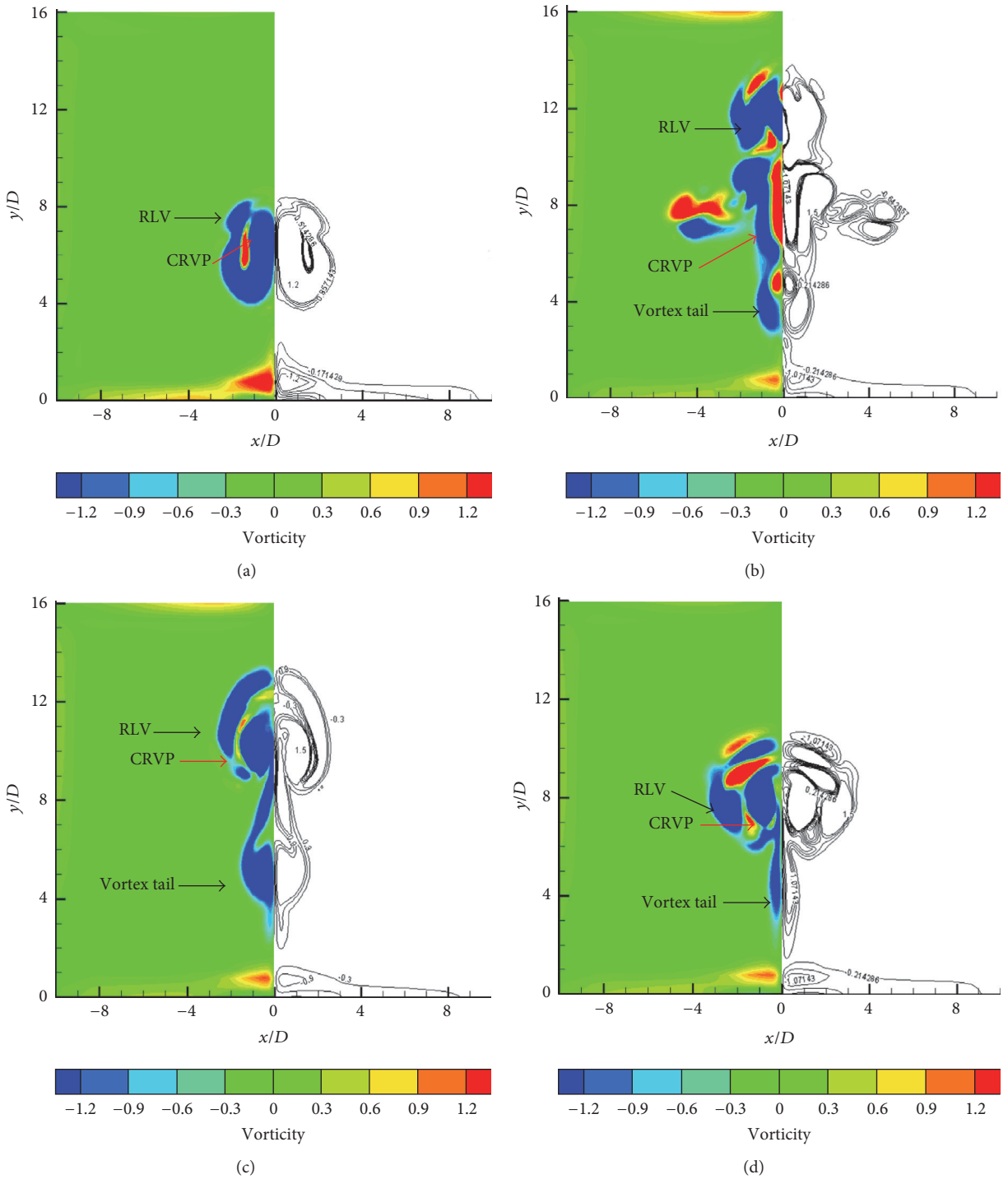

Figure 13: Comparison of time-averaged longitudinal vorticity at $x = 6D$ ((a) C4, (b) C8, (c) C12, and (d) C16 (red: positive vorticity, blue: negative vorticity)).

corresponding position seems to be consistent for the studied cases. Hsu et al. [6] had shown that a vortex called clockwise-rotating vortex appears in the wake side of the jet due to the interaction between the upshear effect induced by the enhanced jet momentum and the downwash effect.

A latent phenomenon is that there is no returning streamline into the nozzle on both the leeward and windward sides near the exit of the nozzle; however, the returning streamlines are generated in the pulsating JICF (Figures 14(b), 14(c), and 14(d)). This is because the velocity profile for the pulsating JICF can generate a large velocity at a certain moment and even demonstrate a small velocity at another moment. This means the velocity profile not only shows the blowing process but also can generate a process of suction. When the velocity

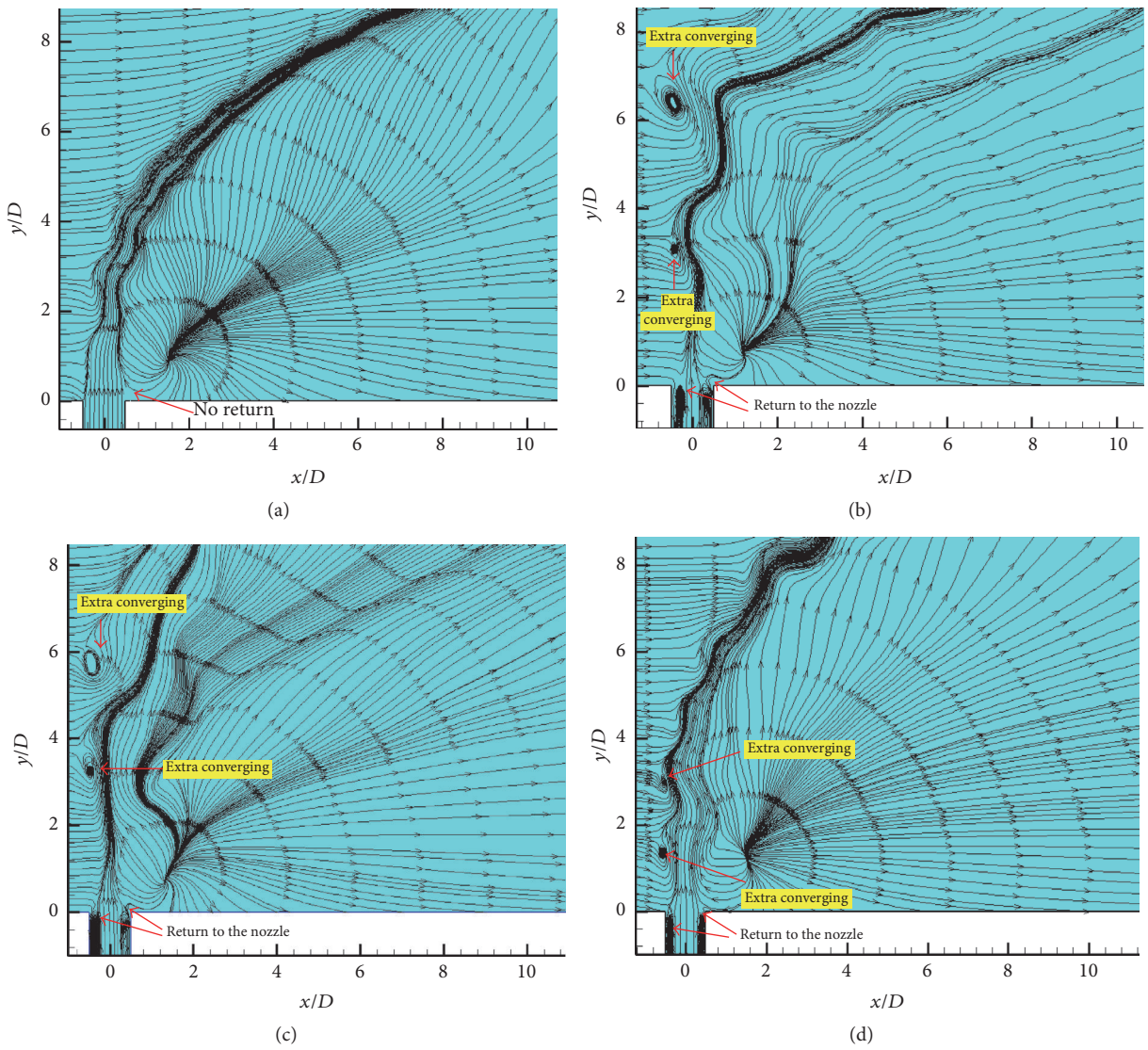

FIGURE 14: Phase-averaged velocity fields near the nozzle at $r = 4$ ((a) C4; (b) C8, C12, and C16).

profile generates a lower value in the process of suction, the fluids near the nozzle exit will return to the nozzle at a certain moment. One more imperceptible phenomenon is found in the pulsating JICF cases. Two extra converging points appear on the windward side of the jet and the position varies at different Strouhal numbers. As the Strouhal number decreases, the corresponding positions are going down.

3.6. Temperature Contours. The nondimensional temperature in JICF can be defined as [30]

$$\theta = \frac{T - T_{cf}}{T_j - T_{cf}}, \tag{9}$$

where T_j and T_{cf} are the temperature of the jet and the crossflow, respectively. The temperature contours on the isosurface for the studied cases based on the same velocity ratio ($r = 3$) are quantitatively compared in Figure 15.

The Strouhal numbers at 0.11, 0.22, and 0.33 are, respectively, investigated to study the effects for the jet mixing in the crossflow created by the various Strouhal number. The colder zone mainly locates on the leeward side of the jet. The compared results demonstrate that the temperature profiles become quite different between the classical JICF and pulsating JICF. In Figure 15(a), the colder zone is regular and stable, while in Figures 15(b), 15(c), and 15(d), the pulsating JICF cases indicate intermittent temperature profiles of the jet. Due to the changing velocity profiles of the pulsating JICF, the temperature profiles of jet have shown a slender shape with the increasing Strouhal number. The colder zone on the leeward side of the pulsating JICF at lower Strouhal numbers will generate a smaller area than the classical JICF. It is obvious that the temperature contours with greater Strouhal numbers can display a similar performance compared with the classical JICF. The predicted temperature profiles have undergone significant changes with the Strouhal number

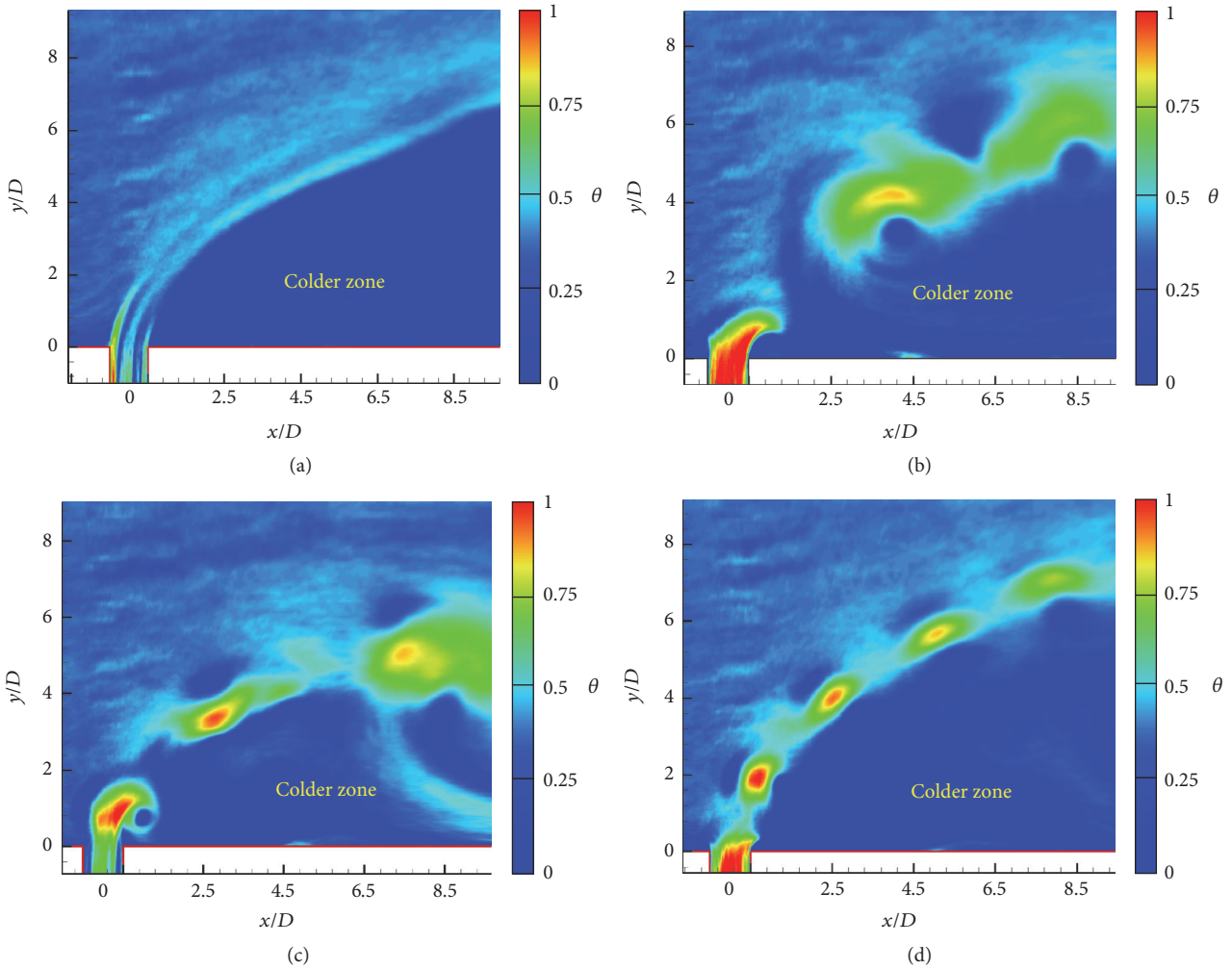

Figure 15: Temperature contours on the iso-surface ((a) C3, (b) C7, (c) C11, and (d) C15).

substantially. For the time-averaged particle trajectories, the pulsating JICF has generated a higher penetration, while the colder zone of the pulsating JICF with relatively lower Strouhal numbers is smaller than the classical JICF. In order to improve the efficiency of the cooling, taking the higher Strouhal number into consideration in the engineering application should be acceptable.

4. Conclusions

In this paper, the flow fields for the classical and pulsating jet in crossflow at low Reynolds number (Re = 100) have been investigated based on LES method. The corresponding conclusions have been listed as follows:

(1) The JICF penetrates higher at higher velocity ratio. The time-averaged particle trajectories of the pulsating JICF can be generated actually higher than the classical JICF. The trajectories of the pulsating JICF show constantly curved performance in the near field. The velocity profiles lead to the obvious results for the classical and pulsating JICF.

(2) The formation mechanism for CRVP is that eddy flows are decomposed due to the effect of pressure gradient near the entrance of the jet. Under the pressure gradient, the vortex diameter will be in rapid expansion, and a pair of counter-rotating vortex can be generated along the JICF direction. The emergence of the vortex tail in the process of JICF at higher velocity ratio is due to the enhanced coactions indicated by the increased jet momentum among the CRVP, UV, and shear layer.

(3) For the time-averaged longitudinal vorticity, the coupling magnitude of positive and negative vorticity differs in the classical and pulsating JICF. Compared with the classical JICF, the generated streamlines for the pulsating JICF in the near field have shown different phenomena. The returning streamlines with two extra converging points can be generated on the windward side of the jet. The corresponding positions have also been various at different Strouhal numbers, while the temperature contours at the greater Strouhal numbers are similar to the classical JICF.

Competing Interests

The authors declare that there is no conflict of interests regarding the publication of this paper.

Authors' Contributions

The individual contributions of authors to the manuscript are specified as follows. (1) Jianlong Chang conceived and designed the simulation. (2) Jianlong Chang, Xudong Shao, and Xiao Hu contributed analysis tools and performed the simulation. (3) Jianlong Chang, Jiangman Li, and Xudong Shao analyzed the data. (4) Jianlong Chang and Jiangman Li wrote the manuscript. (5) Jiangman Li and Xiao Hu helped perform the analysis with constructive discussions.

Acknowledgments

The grant support from the National Science Foundation of China (no. U1430113), Aerospace Light Alloy Components Advanced Manufacturing Innovation Team in North University of China, and 333 Academic Start Funding for Talents in North University of China (no. 13011912) is greatly acknowledged.

References

[1] S. Muppidi and K. Mahesh, "Direct numerical simulation of round turbulent jets in crossflow," *Journal of Fluid Mechanics*, vol. 574, pp. 59–84, 2007.

[2] M. Campolo, M. V. Salvetti, and A. Soldati, "Mechanisms for microparticle dispersion in a jet in crossflow," *AIChE Journal*, vol. 51, no. 1, pp. 28–43, 2005.

[3] S. Srinivasan, R. Pasumarti, and S. Menon, "Large-eddy simulation of pulsed high-speed subsonic jets in a turbulent crossflow," *Journal of Turbulence*, vol. 13, article N1, 2012.

[4] C. M. Hsu and R. F. Huang, "Effects of acoustic excitation at resonance Strouhal numbers on characteristics of an elevated transverse jet," *Experimental Thermal and Fluid Science*, vol. 35, no. 7, pp. 1370–1382, 2011.

[5] C. Marugán-Cruz, J. Rodríguez-Rodríguez, and C. Martínez-Bazán, "Formation regimes of vortex rings in negatively buoyant starting jets," *Journal of Fluid Mechanics*, vol. 716, pp. 470–486, 2013.

[6] C. M. Hsu, R. F. Huang, and M. E. Loretero, "Unsteady flow motions of an oscillating jet in crossflow," *Experimental Thermal and Fluid Science*, vol. 55, pp. 77–85, 2014.

[7] R. Camussi, G. Guj, and A. Stella, "Experimental study of a jet in a crossflow at very low Reynolds number," *Journal of Fluid Mechanics*, vol. 454, pp. 113–144, 2002.

[8] S. Cadirci, H. Gunes, and U. Rist, "Numerical investigation of a jet and vortex actuator in a cross flow boundary layer," *European Journal of Mechanics, B/Fluids*, vol. 44, pp. 42–59, 2014.

[9] S. Bagheri, P. Schlatter, P. J. Schmid, and D. S. Henningson, "Global stability of a jet in crossflow," *Journal of Fluid Mechanics*, vol. 624, pp. 33–44, 2009.

[10] T. T. Lim, T. H. New, and S. C. Luo, "Scaling of trajectories of elliptic jets in crossflow," *AIAA Journal*, vol. 44, no. 12, pp. 3157–3160, 2006.

[11] T. H. New, "Near-field developments of elliptic jets in crossflow," *Journal of Turbulence*, vol. 9, article N24, 2008.

[12] L. L. Yuan, R. L. Street, and J. H. Ferziger, "Large-eddy simulations of a round jet in crossflow," *Journal of Fluid Mechanics*, vol. 379, pp. 71–104, 1999.

[13] C. Cárdenas, R. Suntz, J. A. Denev, and H. Bockhorn, "Two-dimensional estimation of Reynolds-fluxes and -stresses in a Jet-in-Crossflow arrangement by simultaneous 2D-LIF and PIV," *Applied Physics B: Lasers and Optics*, vol. 88, no. 4, pp. 581–591, 2007.

[14] T. H. New, T. T. Lim, and S. C. Luo, "Effects of jet velocity profiles on a round jet in cross-flow," *Experiments in Fluids*, vol. 40, no. 6, pp. 859–875, 2006.

[15] E. J. Gutmark and F. F. Grinstein, "Flow control with noncircular jets," *Annual Review of Fluid Mechanics*, vol. 31, pp. 239–272, 1999.

[16] T. Sikroria, A. Kushari, S. Syed, and J. A. Lovett, "Experimental investigation of liquid jet breakup in a cross flow of a swirling air stream," *Journal of Engineering for Gas Turbines and Power*, vol. 136, no. 6, Article ID 061501, 2014.

[17] O. Hassan and I. Hassan, "Experimental flow-field investigations downstream a scaled-up micro-tangential-jet scheme using the particle image velocimetry technique," *Journal of Fluids Engineering, Transactions of the ASME*, vol. 136, no. 7, Article ID 071204, 2014.

[18] C. Lyko, J. Dähnert, and D. Peitsch, "Forcing of separation bubbles by main flow unsteadiness or pulsed vortex generating jets—a comparison," *Journal of Turbomachinery*, vol. 136, no. 5, Article ID 051016, 2013.

[19] M. Salewski, D. Stankovic, and L. Fuchs, "A comparison of single and multiphase jets in a crossflow using large eddy simulations," *Journal of Engineering for Gas Turbines and Power*, vol. 129, no. 1, pp. 61–68, 2007.

[20] E. M. Ivanova, B. E. Noll, and M. Aigner, "A numerical study on the turbulent schmidt numbers in a jet in crossflow," *Journal of Engineering for Gas Turbines and Power*, vol. 135, no. 1, Article ID 011505, 2013.

[21] E. M. Ivanova, B. E. Noll, and M. Aigner, "Computational modeling of turbulent mixing of a transverse jet," *Journal of Engineering for Gas Turbines and Power*, vol. 133, no. 2, Article ID 021505, 2011.

[22] M. Salewski, D. Stankovic, and L. Fuchs, "Mixing in circular and non-circular jets in crossflow," *Flow, Turbulence and Combustion*, vol. 80, no. 2, pp. 255–283, 2008.

[23] J.-C. Jouhaud, L. Y. M. Gicquel, B. Enaux, and M.-J. Esteve, "Large-Eddy-simulation modeling for aerothermal predictions behind a jet in crossflow," *AIAA Journal*, vol. 45, no. 10, pp. 2438–2447, 2007.

[24] P. Sagaut, *Large Eddy Simulation for Incompressible Flows*, Scientific Computation, Springer-Verlag, 2001.

[25] J. Chang, X. Shao, X. Hu, and S. Zhang, "Flow characteristics of a low reynolds number jet in crossflow with an obstacle block," *The Open Fuels & Energy Science Journal*, vol. 9, no. 1, pp. 37–46, 2016.

[26] S. Muppidi and K. Mahesh, "Study of trajectories of jets in crossflow using direct numerical simulations," *Journal of Fluid Mechanics*, vol. 530, pp. 81–100, 2005.

[27] B. D. Pratte and W. D. Baines, "Profiles of the round turbulent jet in a cross flow," *Journal of the Hydraulics Division*, vol. 93, no. 6, pp. 53–64, 1967.

[28] B. A. Haven and M. Kurosaka, "Kidney and anti-kidney vortices in crossflow jets," *Journal of Fluid Mechanics*, vol. 352, pp. 27–64, 1997.

[29] A. K. Saha and C. B. Yaragani, "Three-dimensional numerical study of jet-in-crossflow characteristics at low Reynolds number," *Heat and Mass Transfer*, vol. 48, no. 2, pp. 391–411, 2012.

[30] G. He, Y. Guo, and A. T. Hsu, "The effect of Schmidt number on turbulent scalar mixing in a jet-in-crossflow," *International Journal of Heat and Mass Transfer*, vol. 42, no. 20, pp. 3727–3738, 1999.